

Design of Green Light Sources Using Nonlinear Photonics and On-Chip Pump Lasers

Chih-Hao Li , Sujit H. Ramachandra, Imad I. Faruque, Sarvagya Dwivedi , *Member, IEEE*,
and Shamsul Arafin , *Senior Member, IEEE*

Abstract—A fully-functional photonic integrated circuit (PIC) platform with supporting active and passive components in the green part of the visible spectral regime is of significant research interest for next-generation optical systems. Here we design highly-integrated ~ 3.5 mm long PICs at green wavelengths, which consist of on-chip GaAs-based near-infrared pump lasers, SiN-LiNbO₃ hybrid waveguides and ring resonators for nonlinear frequency conversion. The waveguides in the PICs are designed to eliminate etching of LiNbO₃, reducing fabrication challenges. Efficient wavelength of 1062 nm pump to 531 nm coherent light is achieved by employing modal phase matching. Unlike a quasi-phase matching technique, modal phase matching enables poling-free operation and further eases device fabrication with comparable performance in terms of second harmonic generation efficiency. The effective nonlinear mode-overlap factor between 1062-nm-TE₀₀ and 531-nm-TE₀₁ modes in the hybrid waveguide is calculated to be 26%. For robust on-chip light coupling between pump laser and waveguide, a calculated maximum coupling efficiency of -2.3 dB is achieved. The theoretical work presented is an initial step towards demonstrating complex non-telecom PICs which could offer a comprehensive range of photonic functionalities.

Index Terms—Photonic integrated circuit, GaAs, silicon nitride, lithium niobate, second harmonic generation, and hybrid integration.

I. INTRODUCTION

THE application and widespread availability of photonic integrated circuits (PICs) are still limited to the narrow telecom band. Recently, non-telecom PICs [1] at near-infrared (NIR) and visible spectral domains have gained considerable attention in order to enable a whole range of emerging applications. PICs operating at green wavelengths are beneficial for biochemical sensing, on-chip holography, underwater communication and quantum technology [2], [3]. Such highly-integrated green

PICs will not only provide low-size, -weight, -power and -cost (SWaP-C) advantages but also bring transformative changes to LiDAR and navigation systems in a GPS-denied environment with precise timing, frequency, and position sensing [4].

Despite the utmost need, green PICs have not yet reached their full potential due to unavailability of highly-efficient chip-compatible green lasers [5]. One of the major technological challenges is to realize high-quality semiconductor laser materials that are suitable for green light generation. GaN and its ternary alloys are one of the obvious choices of gain materials for developing high-performance green lasers at this critical part of the visible spectrum. Broad-area multimode indium-gallium-nitride (InGaIn) laser diodes emitting at 525 nm with 1 Watt of optical power are now commercially available [6]. However, short lifetime and poor reliability of the commercial green lasers due to low-quality In-rich InGaIn essentially limit their usability in integrated platforms [7]–[9]. As an alternative to the InGaIn-based lasers, the generation of green light can be realized using the mature GaAs laser technology and frequency doubling in materials with high nonlinear susceptibility. Such a process is known as second harmonic generation (SHG) where a high intensity optical field interacts with a nonlinear material and generates a new optical field with twice the frequency [10].

As far as nonlinear materials go, it is essential to have a non-centrosymmetric lattice structure in order to achieve SHG. A number of materials including potassium titanyl phosphate (KTP), barium titanate (BaTiO₃), III-V compound semiconductors, and lithium niobate (LiNbO₃) exhibit this key crystal property. Among these materials, LiNbO₃ is an excellent candidate not only for its broadband SHG capability over infrared and visible spectral regimes but also for its large nonlinear tensor [10] and wide optical transparency window [11]. In recent years, high-quality thin-film LiNbO₃ (TFLN)-on-insulator on silicon substrates are commercially available, which allows the development of nonlinear photonic systems even at the chip-scale [12]. Despite significant promise offered by TFLN, patterning and waveguide definition in this material by plasma etching is challenging due to its high etch resistance. It is found that plasma etching of TFLN commonly yields high sidewall roughness, which induces light scattering, and thus relatively high propagation loss [13]. In this work, we study and design integrated hybrid waveguides, composed of TFLN and silicon nitride (SiN), to enable a low-loss platform without the need to etch TFLN.

Manuscript received March 21, 2021; revised May 26, 2021; accepted July 5, 2021. Date of publication July 8, 2021; date of current version August 10, 2021. (Chih-Hao Li and Sujit H. Ramachandra contributed equally to this work.) (Corresponding author: Shamsul Arafin.)

Chih-Hao Li, Sujit H. Ramachandra, and Shamsul Arafin are with the Department of Electrical and Computer Engineering, The Ohio State University, Columbus, OH 43210 USA (e-mail: li.11561@osu.edu; sujit.1@buckeyemail.osu.edu; arafin.1@osu.edu).

Imad I. Faruque is with IPaQS, Heriot-Watt University, EH14 4AS Edinburgh, U.K., and QET Labs, University of Bristol, BS8 1TL, Bristol, U.K. (e-mail: i.faruque@hw.ac.uk).

Sarvagya Dwivedi is with IMEC, Leuven 3001, Belgium (e-mail: sarvagya_dwivedi@ece.ucsb.edu).

Color versions of one or more figures in this article are available at <https://doi.org/10.1109/JSTQE.2021.3095793>.

Digital Object Identifier 10.1109/JSTQE.2021.3095793

Several groups have reported SHG with TFLN through quasi-phase matching (QPM), including TFLN ridge waveguides [14], [15] and TFLN microring resonators [16]. However, QPM requires an elaborate fabrication process where metal deposition for electrodes followed by periodic inversion of the domain polarity in crystals (known as periodic poling) is required. Despite leading to some of the highest reported SHG efficiency values in the TFLN platform [16], QPM is more fabrication demanding and consumes extra electrical power for the poling process. In contrast, modal phase matching (MPM) in TFLN circumvents the poling requirement as it is inherently a better phase matching process. Hence, the poling-free MPM technique requires less fabrication effort which results in a cost-effective solution. Other previously reported MPM-based work includes etched TFLN with strip waveguides [17] and resonator structures [18], [19]. Our theoretical work, for the first time, presents a highly-integrated chip-scale green light source based on the MPM technique to achieve SHG. Specifically, an on-chip GaAs-based pump laser is designed for an emission at a fundamental wavelength of 1062 nm which is then converted to the desired 531 nm light. This green light emission is then collected as useful output into an optical fiber.

II. NONLINEARITY IN WAVEGUIDES AND MODAL DISPERSION

In a SHG process, a fundamental (or pump) optical field and a second harmonic (SH) field interact coherently through a nonlinear material, and the energy from the fundamental is converted to the SH field. The strength of the interaction depends upon a few key factors, such as energy and momentum conservation as well as the nonlinear mode overlap factor [20]. Optimization of these two factors in our design as well as estimation of the conversion efficiency in the SHG process will now be discussed.

A. Energy Conservation and Phase Matching

The energy conservation of SHG entails two pump photons converting into one SH photon. We then have

$$\hbar\omega_P + \hbar\omega_P = \hbar\omega_{SH}, \quad (1)$$

where ω_P and ω_{SH} are the angular frequencies at pump and SH wavelengths, respectively, and \hbar the reduced Planck's constant. Similarly, momentum conservation, also known as phase matching, between the pump and SHG photons is expressed as

$$\hbar \cdot \Delta k = 2\hbar k_P - \hbar k_{SH} = 0, \quad (2)$$

where k_P and k_{SH} are wavevectors at the pump and SH wavelengths, respectively, and Δk is the wavevector mismatch. The wavevector is defined as $k = n_{\text{eff}} \omega / c$, where n_{eff} is the effective refractive index of the waveguide mode for that particular angular frequency ω , and c is the speed of light. Note that perfect phase matching requires $\Delta k = 0$.

In a waveguide, perfect phase matching between pump and SH wavelengths with the same optical mode is not possible owing to waveguide dispersion. Our nonlinear photonic circuit design employed a MPM technique that involves interaction between fundamental modes at the pump wavelength and higher order

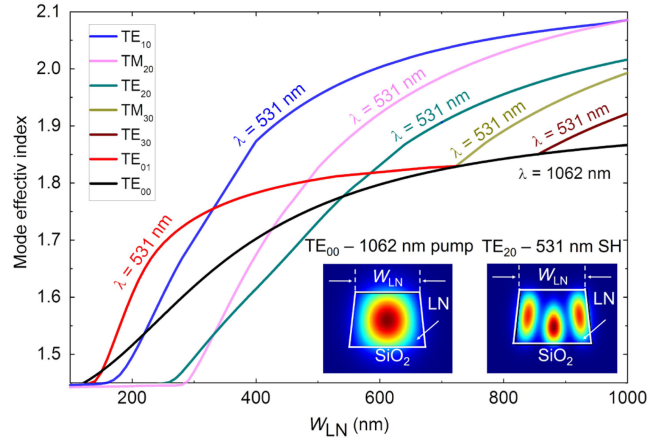


Fig. 1. Mode effective index as a function of W_{LN} . TE_{00} fundamental at 1062 nm and TE_{20} SH mode profiles at 531 nm for the fully-etched TFLN ridge waveguide with $W_{LN} = 540$ nm are shown in the inset.

modes at the SH wavelength. This was done by tuning waveguide dimensions through dispersion engineering. For a specific waveguide size, the mode refractive index n_{eff} of a fundamental mode at the pump wavelength can be phase matched to the n_{eff} of a higher order mode at the SH wavelength as

$$n_{\text{eff,P}}^{\text{FM}}(W, H, \lambda_P) = n_{\text{eff,SH}}^{\text{HM}}(W, H, \lambda_{SH}), \quad (3)$$

where $n_{\text{eff,P}}^{\text{FM}}$ and $n_{\text{eff,SH}}^{\text{HM}}$ are functions of waveguide width W , waveguide height H , and the pump and SH wavelengths, λ_P and λ_{SH} , respectively.

Fig. 1 shows an example of the mode effective index as a function of the top-width W_{LN} of a fully-etched trapezoidal-shaped TFLN waveguide, buried in SiO_2 , at the pump and SH wavelengths of 1062 nm (black line only) and 531 nm, respectively. The TFLN height H_{LN} was set to a fixed value of 320 nm, and W_{LN} was swept from 100 to 1000 nm to calculate n_{eff} . The points of intersection between the mode effective index curves at 1062 nm and 531 nm provide specific W_{LN} values for phase matching. Details on the points at which MPM is attained can be found in Table III of Appendix I. In this design, MPM is observed between the TE_{00} mode at the pump wavelength and the TE_{20} mode at the SH wavelength when $W_{LN} = 540$ nm and $H_{LN} = 320$ nm. These two mode profiles simulated by using Lumerical MODE are also shown in the inset of Fig. 1. Since SHG is a three-wave mixing process, it is important to use nonlinear mode overlap factor [13] to quantify the energy transfer from two fundamental fields to one SH field. Such a factor is proportional to the energy transfer and is used to determine the most efficient MPM solution.

B. Nonlinear Mode Overlap Factor

The nonlinear mode overlap factor (ζ) in a microring resonator structure is given by [20]

$$\zeta = \frac{\int_{\chi^{(2)}} (E_{2i}^{(\text{wg})})^* (E_{1i}^{(\text{wg})})^2 d^2x}{|\int_{\chi^{(2)}} |E_1^{(\text{wg})}|^2 E_1^{(\text{wg})} dx^2|^{2/3} |\int_{\chi^{(2)}} |E_2^{(\text{wg})}|^2 E_2^{(\text{wg})} dx^2|^{1/3}}, \quad (4)$$

where $\int_{\chi}^{(2)}$ is the integral over the entire area of the $\chi^{(2)}$ material. $E_1^{(\text{wg})}$ and $E_2^{(\text{wg})}$ are waveguide mode profiles at the pump and SH wavelengths. $E_{1i}^{(\text{wg})}$ and $E_{2i}^{(\text{wg})}$ are the waveguide mode field components in the $i = x, y,$ or z directions where the dominant SHG takes place due to the highest component of the waveguide material's susceptibility tensor. In (4), there are a few underlying assumptions including the resonator is large enough (i.e., large radius) and the resonator-geometry is symmetric. Both of these conditions are satisfied for our design. The calculated nonlinear mode overlap factor of the TE_{00} and TE_{20} modes, shown in Fig. 1, is 0.08. For other MPM solutions, the value of this factor is listed in Table III of Appendix I.

C. SHG Conversion Efficiency

For high SH optical output, a relatively high field intensity of the fundamental is required in the waveguides. In this study, a microring resonator was used for building up the field intensity. Assuming that the pump is not depleted during SHG, we define a maximum conversion efficiency Γ under continuous-wave operation as [20]

$$\Gamma = \frac{64|\gamma|^2 Q_{1t}^4 Q_{2t}^2}{\hbar\omega_1^4 Q_{1e}^2 Q_{2e}^2}, \quad (5)$$

where Q_{1t} and Q_{1e} (Q_{2t} and Q_{2e}) are Q-factors at the pump (SH) wavelength. The Q-factors are defined as $Q_{t(e)} = \omega/\kappa_{t(e)}$, where κ_t is total cavity loss rate and κ_e the external coupling rate. The coupling strength γ is proportional to ζ in a resonator structure and can be further expressed as [20]

$$\gamma = \sqrt{\frac{\hbar\omega_{10}^2\omega_{20}}{2\tilde{\epsilon}_0\tilde{\epsilon}_1^2\tilde{\epsilon}_2}} \frac{d_{\text{eff}}\zeta}{\sqrt{A_{\text{eff}}^{(\text{wg})}L}}, \quad (6)$$

where ω_{10} (ω_{20}) is the angular frequency of the fundamental (SH) close to the MPM point, $\tilde{\epsilon}_1$ ($\tilde{\epsilon}_2$) the nonlinear material's relative permittivity at the pump (SH) wavelength, ϵ_0 the permittivity of free space, d_{eff} the TFLN's d_{33} element of the susceptibility tensor, $A_{\text{eff}}^{(\text{wg})}$ the waveguide effective area, and L the cavity length. In our design, the MPM process in micro-ring resonators is realized using a hybrid waveguide scheme as discussed in Section III.

III. PASSIVE COMPONENTS

With a SiN-TFLN hybrid waveguide setup, the high nonlinear coefficient of LN is leveraged for wavelength conversion while SiN helps guide light and reduces fabrication complexity. In the following, the design details of all the passive components including MPM-supporting hybrid waveguides and microring resonators will be discussed.

A. Hybrid Waveguide Design

The appropriate material properties, such as crystal orientation and refractive index are crucial for defining hybrid waveguides within nonlinear PICs. Compressively-strained conventional type-I III-V lasers produce TE-polarized light emission. Hence, an X-cut TFLN is chosen with the z -axis of the crystal oriented parallel to the TE mode in order to exploit the d_{33}

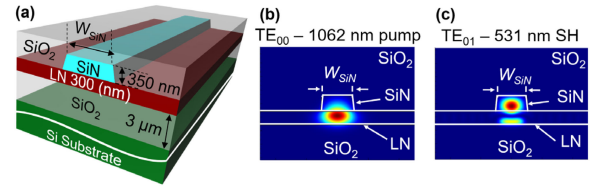


Fig. 2. (a) SiN-TFLN hybrid waveguide. Mode profiles of the (b) TE_{00} fundamental mode at 1062 nm, and (c) TE_{01} SH mode at 531 nm.

component of the second order susceptibility tensor. Additionally, when doped with a sufficient amount of magnesium oxide (MgO), TFLN exhibits an enhancement of resistance to photorefractive damage [21] and suppression of green-induced infrared absorption [22], particularly crucial to our device because of the wavelengths of interest.

To achieve hybrid waveguides based on a two-material core for nonlinear photonics, the second material should have a refractive index close to TFLN. Despite of non-centrosymmetry, SiN as the second hybrid waveguide material is chosen in this study due to its similar refractive index similar to that of TFLN, deposition technology availability and optical transparency in the wavelength range of interest [23]. Similar dispersion of both materials allows engineering the energy distribution of the guided light inside SiN and TFLN by adjusting waveguide dimensions. Material dispersion for TFLN is obtained from [24], where the extraordinary refractive index $n_e \sim 2.15$ at 1062 nm and 2.22 at 531 nm. The refractive index of the SiN at 1062 nm and 531 nm are 1.99 and 2.03, respectively [25].

SiN deposited by low-pressure chemical vapor deposition (LPCVD) is silicon-rich, which increases material absorption in the visible spectrum. Also, high-temperature operation in LPCVD induces cracks on TFLN due to a thermal expansion mismatch between materials, so a rib-loaded SiN-TFLN waveguide structure with unetched TFLN is only viable with a low-temperature plasma enhanced chemical vapor deposition (PECVD) process. Bonding SiN is an alternative integration option, but it will add fabrication complexity. Therefore, our hybrid waveguide is designed with PECVD SiN on top of un-patterned LNOI.

A thin TFLN slab causes a larger fraction of the mode to be guided inside the SiN region, resulting in weak SHG. On the other hand, when TFLN grows thicker, slab modes start to dominate. We then set H_{LN} to 300 nm as available from commercial vendors. The SiN height H_{SiN} involves a trade-off among MPM, propagation loss, and optical power distribution. As H_{SiN} decreases, the optical power distribution in TFLN increases. This is, however, overshadowed by the decrease in MPM-induced nonlinear mode overlap factor and the increase in propagation loss. In contrast, as H_{SiN} increases, the optical power distribution in TFLN decreases. Also, to satisfy MPM in this case, a wider SiN top-width W_{SiN} is needed, which further decreases the power distribution in the TFLN. Based on the above, H_{SiN} is designed to be 350 nm. The simulated mode profiles of the TE_{00} mode at 1062 nm and the TE_{01} mode at 531 nm are shown in Fig. 2(b) and 2(c), respectively.

Fig. 3(a) shows the mode effective index profiles as a function of W_{SiN} within the SiN-TFLN hybrid waveguide at pump

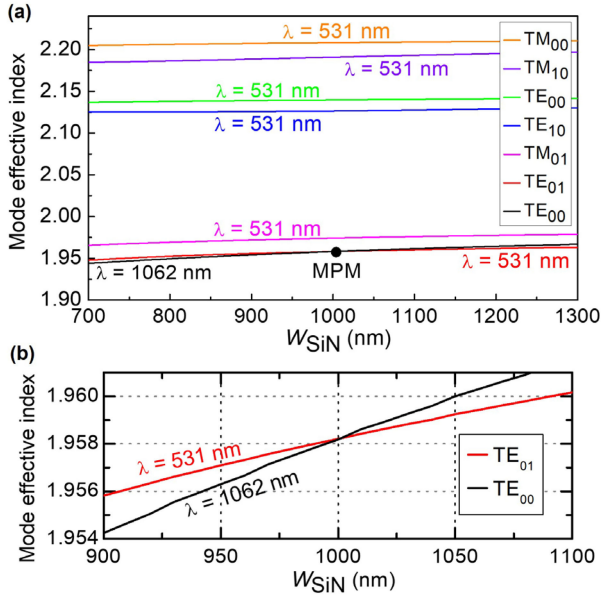


Fig. 3. (a) Mode effective index in SiN-TFLN hybrid waveguide as a function of W_{SiN} , and (b) expanded view of the mode effective index as a function of W_{SiN} around the MPM point, where $W_{SiN} = 1000$ nm, $H_{SiN} = 350$ nm, and $H_{LN} = 300$ nm.

TABLE I
A COMPARISON BETWEEN THE MPM SOLUTIONS OF THE DESIGNED HYBRID- AND TFLN RIDGE WAVEGUIDE BURIED IN SILICON DIOXIDE

| Property | SiN-TFLN Hybrid Waveguide | TFLN Ridge Waveguide |
|--------------------------|---------------------------|----------------------|
| Mode at 531 nm | TE_{01} | TE_{20} |
| n_{eff} | 1.96 | 1.78 |
| H_{LN} (nm) | 300 | 320 |
| Waveguide top width (nm) | $W_{SiN} = 1000$ | $W_{LN} = 540$ |
| ζ | 0.26 | 0.08 |

1062 nm (black line only) and SH 531 nm. Unlike the mode effective index curves in Fig. 1, the curves here are relatively flat. Achieving MPM with the TE_{00} mode at 1062 nm is therefore limited to TE_{01} mode at 531 nm. Fig. 3(b) shows the zoom-in MPM point ($W_{SiN} = 1000$ nm, $H_{SiN} = 350$ nm, and $H_{LN} = 300$ nm) of the TE_{00} and TE_{01} modes. In our designed hybrid waveguide, the 3-dB SHG phase matching bandwidth centering at the pump wavelength is calculated to be 1.9 nm. Table I gives a comparison between the MPM solutions of our designed hybrid waveguide and the fully-etched TFLN ridge waveguide shown in Fig. 1. MPM at TE_{20} mode in the ridge is selected for comparison because of its highest nonlinear mode overlap factor as shown in Table III (see Appendix I). Note that the overlap factor in the SiN-TFLN hybrid waveguide is more than three times higher than the that of the TFLN ridge waveguide. The difference in the values of ζ can be explained by the polarity of the SH field [26].

Our MPM solutions can be explained in terms of the intensity distribution of the mode profiles. The TE_{00} mode profile has a single lobe of intensity distribution and its n_{eff} varies less with respect to different waveguide size. However, higher order modes'

TABLE II
DIFFERENT PARAMETERS OF THE DESIGNED HYBRID MICRORING RESONATOR AND MPM INFORMATION

| Parameter | Designed Value |
|----------------------------|-----------------------------------|
| $W_{SiN} \times H_{SiN}$ | 1000 nm \times 350 nm |
| Slab LN thickness | 300 nm |
| Coupling gap | 720 nm |
| R | ~ 74 μ m |
| FSR around pump wavelength | ~ 1.1 nm |
| FSR around SH wavelength | ~ 0.27 nm |
| FWHM at pump wavelength | 5.1 pm |
| FWHM at SH wavelength | 5.3 pm |
| Q_L at pump wavelength | 2.1×10^5 |
| Q_L at SH wavelength | 2×10^5 |
| κ | 0.12 |
| MPM | TE_{00} (pump) – TE_{01} (SH) |
| Theoretical SHG efficiency | 104,472%/W |

profiles have more than one lobe of intensity distributions, resulting in a stronger dependence of n_{eff} on waveguide dimensions. For instance, TE_{20} mode has three lobes and they are mostly in the TFLN region, which greatly increases n_{eff} because of the higher refractive index of LN. The TE_{01} mode has two lobes as shown in Fig. 2(c), one in SiN and the other in TFLN. Such a distribution is strongly dependent on the waveguide dimensions and makes it easier to fine tune n_{eff} , facilitating MPM. Note that our device can be adapted for applications at different visible wavelengths by changing the waveguide dimensions, given the operating wavelengths are within the optical transparency window of our selected materials.

B. Microring Resonator Design

To enhance the SHG efficiency, the microring resonator should be designed to be doubly resonant at the pump and SH wavelengths. The design process begins with the selection of an appropriate value for the free spectral range (FSR). The choice of the FSR directly impacts the radius R of the microring as

$$R = \frac{\lambda_{res}^2}{2\pi n_g \times \text{FSR}}, \quad (7)$$

where λ_{res} is the resonant wavelength, and n_g is the group index. Large values of FSR yield smaller ring radii, which leads to higher losses due to tighter waveguide bends, but smaller FSR values lead to larger device dimensions.

To account for the impact of the ring curvature on the cross-coupling coefficient κ , piecewise integration of the κ is performed over a length of the bus waveguide. The transfer matrix T_i of each piecewise element i of the coupled waveguide depends on n_{eff} of the even and odd modes (see Appendix II). Fig. 3(a) shows the n_{eff} of these two modes as a function of the coupling gap. Since the dimensions of the cross section of the microring resonator and the waveguide are identical, the even and odd n_{eff} can be fit into exponential equations given by [27]

$$n_E \simeq n_{eff, \text{fund.}} + a_E e^{-\gamma_E g}, \quad (8)$$

$$n_O \simeq n_{eff, \text{fund.}} - a_O e^{-\gamma_O g}, \quad (9)$$

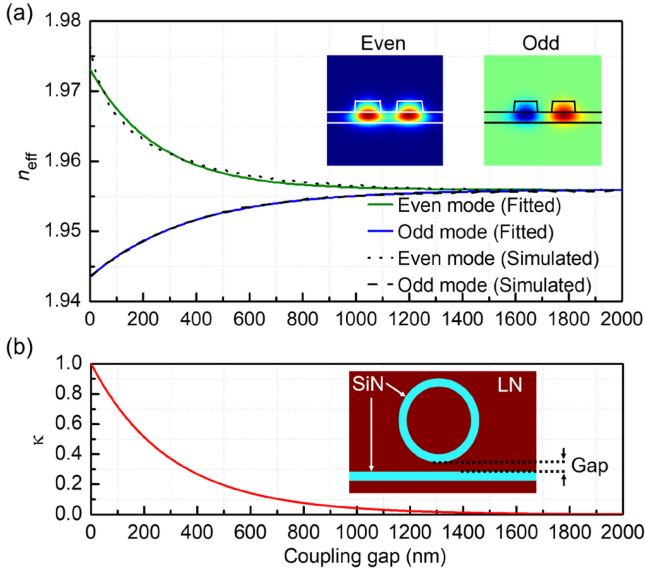


Fig. 4. (a) n_{eff} for even and odd modes as a function of coupling gap; the two modes at a coupling gap of 720 nm are shown as inset, and (b) κ as a function of coupling gap.

where n_E and n_O are the effective refractive indices of the even and odd modes. $n_{\text{eff, fund}}$ is the effective refractive index of the fundamental mode in the waveguide without coupling, g the coupling gap between the ring and the bus waveguide, and d the minimum coupling gap. $\alpha_{E(O)}$ and $\gamma_{E(O)}$ are wavelength dependent positive numbers used for fitting. Here, $n_{\text{eff-fund}} \sim 1.75$, $\alpha_E \sim 0.09$, $\alpha_O \sim 0.04$, $\gamma_E \sim 8$, $\gamma_O \sim 5.5$.

As the gap increases to 2 μm , the waveguide and the ring are spaced far apart and there is negligible coupling between them. This is confirmed by n_{eff} of the even and odd modes converging at larger gap to equal the index of the fundamental mode in either of the waveguides. Examples of the two mode profiles at a gap of 720 nm are shown in the inset. Fig. 4(b) shows κ as a function of the coupling gap, and a schematic of the resonator and waveguide is shown in the inset. Appendix II provides the calculation details of κ .

An all-pass resonator configuration is used to achieve a higher loaded quality factor Q as opposed to an add-drop [28]. The Q -factor scales with λ_{res} and the full width at half maximum (FWHM) as

$$Q_L = \frac{\lambda_{\text{res}}}{\text{FWHM}}, \quad (10)$$

where Q_L is the loaded Q -factor. Figs. 5(a) and (b) show the transmission spectra of the SiN-TFLN hybrid microring structure resonant at both pump and SH wavelengths with FSRs of ~ 1.1 nm and ~ 0.27 nm, respectively, as shown in Figs. 5(c) and (d). Table II summarizes the results obtained from the microring resonator design.

In our design, waveguide losses, including propagation and bending losses, are estimated to be 0.8 dB/cm and 5.5 dB/cm at ~ 1100 nm and ~ 531 nm, respectively. These theoretical values are four times higher, on a log scale, than the reported values in [29]. Hence, the design is adequately conservative as the practical waveguide loss depends strongly on sidewall roughness

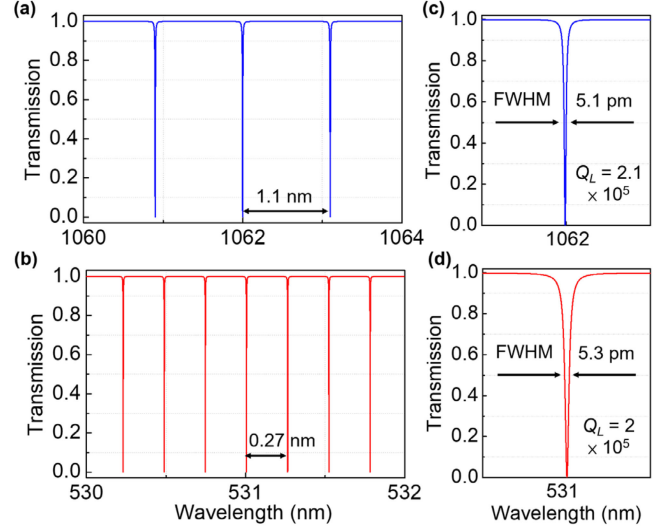


Fig. 5. Simulated transmission spectra of the hybrid microring resonator around the (a) pump and (b) SH wavelengths, and expanded view of the resonances at (c) 1062 nm and (d) 531 nm.

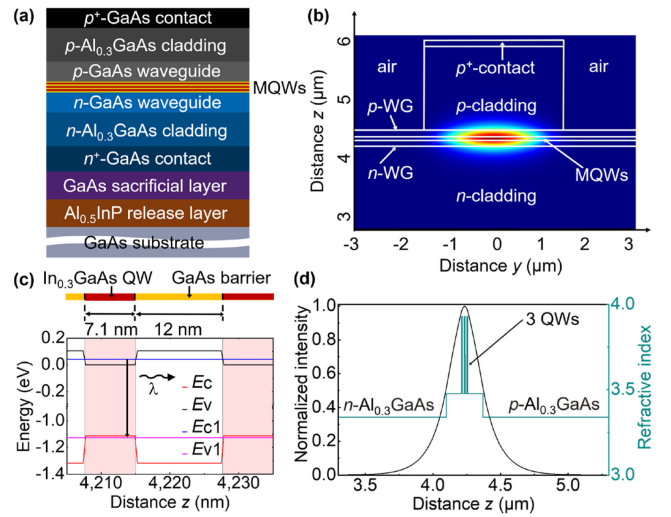


Fig. 6. (a) Epilayer stack of a GaAs-based edge-emitting laser at 1062 nm, (b) fundamental TE mode profile of the laser, (c) energy level profile of the MQWs active region in the growth direction with emission wavelength at 1062 nm, and (d) mode intensity distribution and refractive index profile in the growth direction.

and the actual shape of the resonator. For simplicity, a circular microring resonator structure is used. A more fabrication tolerant structure using a pulley-coupled ring resonator [30] can be used to improve the performance.

IV. ACTIVE COMPONENTS

A GaAs-based edge-emitting laser is designed for light emission at 1062 nm and its cross section is shown in Fig. 6(a). Fig. 6(b) shows the simulated fundamental TE mode in the laser with a ridge width of 3 μm for optical mode guiding. Fig. 6(c) presents the energy level profile in the multiple quantum wells (MQWs) along the growth direction. The active region consists of three QWs of 7.1 nm $\text{In}_{0.3}\text{GaAs}$. This value is close to the calculated critical thickness, but similar thicknesses were

successfully demonstrated by Sundgren *et al.* [31]. The GaAs barriers having a thickness of 12 nm result in compressive strain of 2.2%. The confinement factor Γ is calculated to further assess the optical mode guiding ability of the laser structure. The calculated Γ in the undoped 3 QWs, waveguide layers, p - & n -cladding, and p - & n -contact layers are 5.8%, 44.2%, 36.5%, and $3.5 \times 10^{-4}\%$, respectively. The intensity distribution and refractive index profile are shown in Fig. 6(d).

V. HYBRID INTEGRATION

By integrating the designed laser onto the same chip with the hybrid waveguide components, pump source is readily available. To realize on-chip integration of a laser, transfer printing strategy [32] is selected. This allows the testing of the laser prior to the transfer and enables tight integration. The laser will be initially grown on a GaAs substrate as previously mentioned in Fig. 6(a). The laser will then be detached from the substrate and release layer by selectively etching $\text{Al}_{0.5}\text{In}_{0.5}\text{P}$. Meanwhile, the GaAs sacrificial layer protects the n^+ -contact layer from potential damages which would be detrimental to forming an ohmic contact. The laser is subsequently transferred and bonded to the nonlinear platform with predefined waveguide components as shown in Fig. 7(a). In the following sections, our light coupling strategy as well as the optical power budget will be discussed.

A. Coupling Strategy

Fig. 7(a) shows the 3D schematic of our designed hybrid integration strategy. The designed GaAs laser has a ridge length of ~ 1 mm. The GaAs-based laser tip and the hybrid waveguide's end (adjacent to the laser side) are both tapered down in width. The n -side bottom contact should be formed as an intracavity contact. Importantly, n -contact electrodes will need to be spaced apart from the etched ridges to circumvent the potential facet contamination issue. Light is coupled in and out of the hybrid waveguide region through its edges. The effective index of the TE_{00} mode in the laser waveguide is 3.41. In the hybrid waveguide, this value becomes 1.96 for the same mode at the pump wavelength. This index mismatch together with mode-mismatch are the main causes of on-chip coupling losses.

An efficient transfer of the mode from the laser requires adiabatic tapers for mode transformation. We aim to minimize the effective refractive index difference Δn_{eff} of the TE_{00} modes to reduce reflections at the active-passive interfaces. Therefore, the hybrid waveguide part was gradually tapered down to 700 nm, whereas the laser was tapered to a tip width of 175 nm. This results in $\Delta n_{\text{eff}} = 0.03$. Fig. 7(b) shows the on-chip laser-to-waveguide coupling efficiency with respect to the tapered laser length at zero gap between the tips of the laser and hybrid waveguide. A maximum coupling efficiency of -2.3 dB is achieved with a taper length of $20 \mu\text{m}$ of the hybrid waveguide and $200 \mu\text{m}$ of the laser. The side view of the on-chip laser coupling region is shown in the inset of Fig. 7(b). The lateral and vertical misalignments between the tapered hybrid waveguide and the tapered laser, at zero gap between the tips of the laser and hybrid waveguide, is shown in Fig. 7(c). The coupling efficiency in the z -direction is asymmetric since the hybrid waveguide has a ridge shape in that direction. Fig. 7(d) shows the laser-to-waveguide

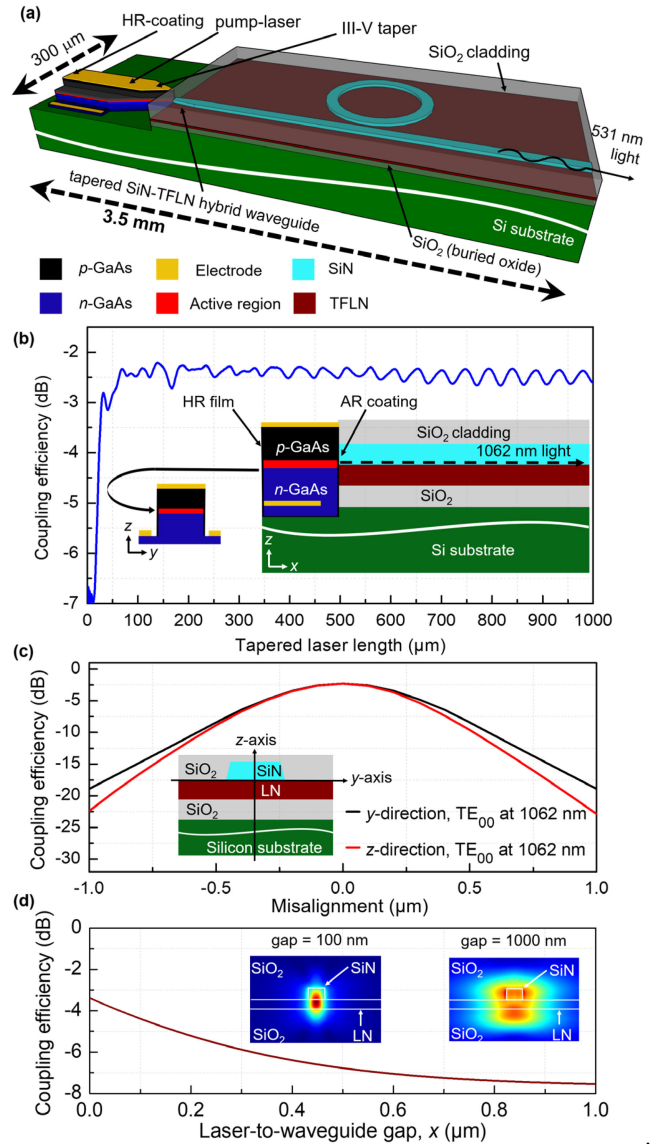


Fig. 7. (a) 3D schematic of the designed device, (b) on-chip laser-to-waveguide coupling efficiency as a function of the tapered laser length. The laser-to-waveguide gap is zero. A side view schematic of the on-chip light coupling strategy is shown as inset, and coupling efficiencies as a function of positional misalignment between the tapered hybrid waveguide and tapered laser in (c) y - and z -directions with zero laser-to-waveguide gap and in (d) coupling gap x directions.

coupling efficiency when a gap between the tips of the laser and hybrid waveguide exists. The coupled fundamental TE mode profiles at the hybrid waveguide tip with laser-to-waveguide gaps of 100 nm and 1000 nm are shown in the insets of Fig. 7(d). As can be seen, the coupling efficiency, approaching the zero laser-to-waveguide gap, is reasonably lower than the value calculated at the zero gap in Fig. 7(c). This is because the results in Fig. 7(d) are obtained from the more accurate 3D finite-difference time-domain (FDTD) method. Figs. 8(a) and (b) show the simulation of the light propagation from the tapered laser to the tapered waveguide, with zero misalignment and zero gap, from the top and side view, respectively.

Off-chip edge coupling requires post-fabrication dicing of a device and possibly a successive polishing step. However,

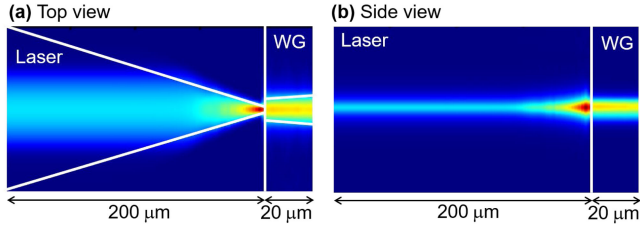


Fig. 8. (a) Top view and (b) side view of the simulation of light propagation from the tapered III-V laser to the tapered hybrid waveguide at the zero laser-to-waveguide gap.

this strategy provides a wider coupling bandwidth, higher efficiency, and lower back reflection than the approach based on a wavelength-selective grating coupler. Hence, the edge coupling strategy is selected to reduce the loss factors detrimental to the measurement of the SHG. It is worth noting that for the target optical output power of 100 mW of GaAs pump lasers with a ridge length of ~ 1 mm, the overestimated driving current should be on the order of only 300 mA and it is expected that there will be minimal self-heating with the pump laser.

B. Power Budget

Optical power loss in the integrated devices stems from on- and off-chip coupling loss, waveguide loss, and a SHG conversion efficiency of less than 100%. The total coupling loss is estimated to be 7.3 dB, which includes minimum coupling loss of 2.3 dB from laser-to-waveguide and outcoupling loss of 5 dB. As mentioned, the waveguide losses at the pump and SH wavelengths are estimated to be four times higher, on a log scale, than the reported values in [29]. Considering these loss values, a SHG conversion efficiency in the range of 1-10% under the condition of undepleted pump approximation, and 100 mW of optical power from the on-chip pump laser, our designed nonlinear PICs are expected to provide an off-chip power of 0.16 - 1.5 mW.

VI. CONCLUSION

In summary, this paper introduces a compact and reliable integration concept for realizing green laser emitters, consisting of on-chip pump sources, low-loss SiN-TFLN hybrid waveguides, and microring resonators. All the active-passive components can be integrated in the proposed fabrication-friendly and low-cost platform to develop single chip solutions. The PICs with a size of $3.5 \text{ mm} \times 300 \text{ } \mu\text{m}$ allows on-chip hybrid coupling of the pump source to the SHG device without using any external optics. In order to extend the chip functionality, the microring resonators can be engineered with top metal heaters for wavelength tuning and side electrodes for electro-optic modulation. This highly-integrated visible nonlinear photonics platform is expected to support new classes of applications including nonlinear, traditional and quantum photonic devices in the UV-NIR wavelength range. Hence, our solutions with low-loss waveguides, reduced power consumption and footprint make it possible to generate large-area chips for green light manipulation beyond generation,

TABLE III
MPM SOLUTIONS OF A FULLY-ETCHED TFLN RIDGE WAVEGUIDE BURIED IN SILICON DIOXIDE

| Mode | n_{eff} at 531 nm | W_{LN} (nm) | ζ |
|------------------|----------------------------|----------------------|----------|
| TE ₁₀ | 1.54 | 220 | ~ 0 |
| TE ₂₀ | 1.78 | 540 | 0.08 |
| TE ₃₀ | 1.85 | 856 | ~ 0 |
| TE ₀₁ | 1.83 | 729 | 0.02 |

that holds high promises for the multi-functional visible PICs in the near future.

APPENDIX I

Table III shows n_{eff} of the higher order TE modes, available for phase matching at 531 nm. The fully-etched TFLN ridge waveguide has a fixed H_{LN} of 320 nm. The TE₂₀ SH mode offers the highest nonlinear mode overlap factor as discussed in Section III and thus, is the best higher order mode for MPM with TE₀₀ mode at 1062 nm in such a waveguide architecture.

APPENDIX II

When integrating κ piecewise over a length of the bus waveguide, each section of the length (Δz) is treated as a system of coupled waveguides. The transfer matrix (T_i) of the i^{th} section is given by [27]

$$T_i = e^{-j\phi_i} \begin{bmatrix} t_i & -j\kappa_i \\ -j\kappa_i & t_i \end{bmatrix}, \quad (\text{A1})$$

where,

$$\phi_i = \frac{2\pi}{\lambda} \Delta z \frac{n_E(g) + n_O(g)}{2}, \quad (\text{A2})$$

$$t_i = \cos \left(\frac{2\pi}{\lambda} \Delta z \frac{n_E(g) - n_O(g)}{2} \right), \quad (\text{A3})$$

$$\kappa_i = \sin \left(\frac{2\pi}{\lambda} \Delta z \frac{n_E(z) - n_O(z)}{2} \right), \quad (\text{A4})$$

where the effective refractive indices of even modes $n_E(g)$ and odd modes $n_O(g)$ are dependent on the coupling gap (g), and t_i is the through coupling coefficient of the i^{th} section. The integrated κ is given by [27]

$$\kappa = \sin \left(\frac{\pi}{\lambda} \left[\frac{a_E}{\gamma_E} e^{-\gamma_E d} B \left(\gamma_E R + \frac{\gamma_E w}{2} \right) + \frac{a_O}{\gamma_O} e^{-\gamma_O d} B \left(\gamma_O R + \frac{\gamma_O w}{2} \right) \right] \right), \quad (\text{A5})$$

where $a_{E(O)}$ and $\gamma_{E(O)}$ are wavelength dependent positive fitting parameters. λ is the wavelength in μm , w the width of the cross section of the ring, and $B(x)$ the curvature function of the coupling region as [27]

$$B(x) = 2x \int_0^{\pi/2} e^{-x(1-\cos\theta)} \cos\theta d\theta, \quad (\text{A6})$$

where θ is the angle between the perpendicular to the waveguide from the center of the ring and the position vector of the length element under consideration.

REFERENCES

- [1] R. Arefin *et al.*, "III-N/SiN integrated photonics platform for blue wavelengths," *IEEE J. Quantum Electron.*, vol. 56, no. 4, pp. 1–9, Aug. 2020.
- [2] G. Giuliano *et al.*, "Laser based underwater communication systems," in *Proc. 18th Intl. Conf. Transparent Opt. Net.*, 2016, pp. 1–4.
- [3] A. J. Antończak, P. Koziol, J. Z. Sotor, P. R. Kaczmarek, and K. M. Abramski, "Laser doppler vibrometry with a single-frequency microchip green laser," *Meas. Sci. Technol.*, vol. 22, no. 11, 2011, Art. no. 115306.
- [4] A. D. Ludlow, M. M. Boyd, J. Ye, E. Peik, and P. O. Schmidt, "Optical atomic clocks," *Rev. Mod. Phys.*, vol. 87, no. 2, pp. 637–701, Jun. 2015.
- [5] J. A. Holguín-Lerma, T. K. Ng, and B. S. Ooi, "Narrow-line InGaN/GaN green laser diode with high-order distributed-feedback surface grating," *Appl. Phys. Exp.*, vol. 12, no. 4, 2019, Art. no. 042007.
- [6] Nichia - LASER Diode (Products). [Online]. Available: https://www.nichia.co.jp/en/about_nichia/index.html.
- [7] H. Xiu, P. Xu, P. Wen, Y. Zhang, and J. Yang, "Rapid degradation of InGaN/GaN green laser diodes," *Superlattices Microstructures*, vol. 142, Apr. 2020, Art. no. 106517.
- [8] T. Miyoshi *et al.*, "510–515 nm InGaN-based green laser diodes on c-plane GaN substrate," *Appl. Phys. Exp.*, vol. 2, May 2009, Art. no. 062201.
- [9] M. Marioli *et al.*, "Degradation mechanisms and lifetime of state-of-the-art green laser diodes," *Phys. Status Solidi A*, vol. 212, pp. 974–979, 2015.
- [10] R. Boyd, *Nonlinear Optics*, 3rd ed., New York, NY, USA: Academic, 2008.
- [11] K. K. Wong, *Properties of Lithium Niobate*, London: Institution of Engineering and Technology, 2002.
- [12] NanoLN - LNOI (Products). [Online]. Available: <https://www.nanoln.com/>
- [13] A. Boes, B. Corcoran, L. Chang, J. Bowers, and A. Mitchell, "Status and potential of lithium niobate on insulator (LNOI) for photonic integrated circuits," *Laser Photon. Rev.*, vol. 12, no. 4, Apr. 2018, Art. no. 1700256.
- [14] C. Wang *et al.*, "Ultra-high efficiency wavelength conversion in nanophotonic periodically poled lithium niobate waveguides," *Optica*, vol. 5, no. 11, pp. 1438–1441, Nov. 2018.
- [15] A. Rao *et al.*, "Actively-monitored periodic-poling in thin-film lithium niobate photonic waveguides with ultrahigh nonlinear conversion efficiency of $4600\%W^{-1}cm^{-2}$," *Opt. Exp.*, vol. 27, no. 18, pp. 25920–25930, Sep. 2019.
- [16] J. J. Lu *et al.*, "Periodically poled thin-film lithium niobate microring resonators with a second-harmonic generation efficiency of $250,000\%/W$," *Optica*, vol. 6, no. 12, pp. 1455–1460, Dec. 2019.
- [17] C. Wang *et al.*, "Second harmonic generation in nano-structured thin-film lithium niobate waveguides," *Opt. Exp.*, vol. 25, no. 6, pp. 6963–6973, Mar. 2017.
- [18] J. Y. Chen, Y. M. Sua, H. Fan, and Y. P. Huang, "Modal phase matched lithium niobate nanocircuits for integrated nonlinear photonics," *OSA Continuum*, vol. 1, no. 1, pp. 229–242, Sep. 2018.
- [19] S. Liu, Y. Zheng, and X. Chen, "Cascading second-order nonlinear processes in a lithium niobate-on-insulator microdisk," *Opt. Lett.*, vol. 42, no. 18, pp. 3626–3629, Sep. 2017.
- [20] R. Luo *et al.*, "Optical parametric generation in a lithium niobate microring with modal phase matching," *Phys. Rev. Appl.*, vol. 11, no. 3, Mar. 2019.
- [21] D. A. Bryan, R. Gerson, and H. E. Tomaschke, "Increased optical damage resistance in lithium niobate," *Appl. Phys. Lett.*, vol. 44, no. 9, pp. 847–849, 1984.
- [22] Y. Furukawa *et al.*, "Green-induced infrared absorption in MgO doped $LiNbO_3$," *Appl. Phys. Lett.*, vol. 78, no. 14, pp. 1970–1972, Apr. 2001.
- [23] R. Baets *et al.*, "Silicon photonics: Silicon nitride versus silicon-on-insulator," in *Proc. Opt. Fiber Commun. Conf.*, 2016, pp. 1–3.
- [24] O. Gayer, Z. Sacks, E. Galun, and A. Arie, "Temperature and wavelength dependent refractive index equations for mgo-doped congruent and stoichiometric $LiNbO_3$," *Appl. Phys. B: Lasers Opt.*, vol. 91, no. 2, pp. 343–348, May 2008.
- [25] H. R. Philipp, "Optical properties of silicon nitride," *J. Electrochem. Soc.*, vol. 120, no. 2, pp. 295–300, 1973.
- [26] R. Luo, Y. He, H. Liang, M. Li, and Q. Lin, "Semi-nonlinear nanophotonic waveguides for highly efficient second-harmonic generation," *Laser Photon. Rev.*, vol. 13, no. 3, 2019, Art. no. 1800288.
- [27] M. Bahadori *et al.*, "Design space exploration of microring resonators in silicon photonic interconnects: Impact of the ring curvature," *J. Lightw. Technol.*, vol. 36, no. 13, pp. 2767–2782, 2018.

- [28] W. Bogaerts *et al.*, "Silicon microring resonators," *Laser Photon. Rev.*, vol. 6, no. 1, pp. 47–73, 2012.
- [29] S. S. Saseendran *et al.*, "A 300mm CMOS-compatible PECVD silicon nitride platform for integrated photonics with low loss and low process induced phase variation," in *Proc. Opt. Fiber Commun. Conf.*, 2019, pp. 1–3.
- [30] D.-P. Cai *et al.*, "Compact pulley-type microring resonator with high quality factor," *Appl. Phys. Exp.*, vol. 7, no. 11, Oct. 2014, Art. no. 112202.
- [31] P. Sundgren, J. Berggren, P. Goldman, and M. Hammar, "Highly strained ingaas/gaas multiple quantum-wells for laser applications in the 1200–1300 nm wavelength regime," *Appl. Phys. Lett.*, vol. 87, no. 7, Aug. 2005.
- [32] B. Corbett, R. Loi, W. D. Zhou, D. Liu, and Z. Q. Ma, "Transfer print techniques for heterogeneous integration of photonic components," *Prog. Quantum Electron.*, vol. 52, pp. 1–17, Mar. 2017.

Chih-Hao Li received the B.S. degree in electrical engineering from National Chung Hsing University, Taichung, Taiwan and the M.S. degree in optics and photonics from the University of Central Florida, Orlando, FL, USA. He is currently working toward the Ph.D. degree with The Ohio State University, Columbus, OH, USA. His current research interests include photonic integrated circuits, nonlinear optics, and semiconductor lasers.

Sujit Ramachandra received the B.E. degree from the R.V College of Engineering, Bangalore, India and the M.S. degree in electrical and computer engineering from The Ohio State University, Columbus, OH, USA. He is currently with industry. His research interests include silicon photonics, lasers, nonlinear optics, and integrated optics.



Imad I. Faruque received the B.Sc. degree in electrical and electronic engineering from the Bangladesh University of Engineering and Technology, Dhaka, Bangladesh, in 2009, the joint Erasmus Mundus Master of Science degree in photonics from Universiteit Gent, Ghent, Belgium, Vrije Universiteit Brussel, Ixelles, Belgium, University of St Andrews, St Andrews, U.K., and Heriot-Watt University, Edinburgh, U.K., and the Ph.D. degree from Quantum Engineering Technology Laboratory, University of Bristol, Bristol, U.K., in 2018. During the Ph.D. degree, he

worked on heralded single-photon sources in silicon photonics, and afterwards as a Postdoc he worked on various quantum communication and quantum metrology projects. He is currently a Postdoctoral Research Associate with Heriot-Watt University, U.K. His research focuses on solving global challenges using quantum technology. He is a Member of OSA.



Sarvagya Dwivedi (Member, IEEE) received the master's degree in electrical engineering from the Indian Institute of Technology, Bombay, Mumbai, India and the joint Ph.D. degree in photonics engineering from the Photonics Research Group, Ghent University, Ghent, Belgium and Imec, Leuven, Belgium. He was a Postdoc Research Associate with the University of California Santa Barbara, Santa Barbara, CA, USA. He has more than nine years of experience in the areas of all-silicon, silicon nitride and Ge-on-Si based tolerant devices and circuits for various applications like datacom, telecom, and mid-infrared sensing and has authored and coauthored more than 40 publications. He is currently a Senior Photonics Researcher with Imec, Belgium, where he is developing optical phased arrays for beamforming, LiDAR, and imaging applications. He is a Member of the OSA and IEEE Photonics Society.



Shamsul Arafin (Senior Member, IEEE) is currently an Assistant Professor with the Electrical and Computer Engineering Department, The Ohio State University, Columbus, OH, USA. He has more than 13 years of experience on the design, fabrication of widely tunable semiconductor lasers, including vertical-cavity surface emitting lasers. He has authored or coauthored more than 120 publications in the areas of III-V materials, the corresponding devices and InP-based photonic integrated circuits and has given numerous invited and contributed talks at various international conferences. He is a Senior Member of the OSA and SPIE.